



Article

# Results and Perspectives of Timepix Detectors in Space—From Radiation Monitoring in Low Earth Orbit to Astroparticle Physics

Benedikt Bergmann <sup>1,\*</sup> , Stefan Gohl <sup>1,2,\*</sup> , Declan Garvey <sup>1</sup> , Jindřich Jelínek <sup>1,3</sup> and Petr Smolyanskiy <sup>1</sup>

<sup>1</sup> Institute of Experimental and Applied Physics, Czech Technical University in Prague, 11000 Prague, Czech Republic; declan.garvey@cvut.cz (D.G.); jindrich.jelinek@etu.unige.ch (J.J.)

<sup>2</sup> Faculty of Mathematics and Physics, Charles University, 18000 Prague, Czech Republic

<sup>3</sup> Department of Nuclear and Particle Physics, University of Geneva, CH-1211 Geneva, Switzerland

\* Correspondence: benedikt.bergmann@utef.cvut.cz (B.B.); stefan.gohl@utef.cvut.cz (S.G.); Tel.: +420-775-868-794 (B.B.)

**Abstract:** In space application, hybrid pixel detectors of the Timepix family have been considered mainly for the measurement of radiation levels and dosimetry in low earth orbits. Using the example of the Space Application of Timepix Radiation Monitor (SATRAM), we demonstrate the unique capabilities of Timepix-based miniaturized radiation detectors for particle separation. We present the incident proton energy spectrum in the geographic location of SAA obtained by using Bayesian unfolding of the stopping power spectrum measured with a single-layer Timepix. We assess the measurement stability and the resiliency of the detector to the space environment, thereby demonstrating that even though degradation is observed, data quality has not been affected significantly over more than 10 years. Based on the SATRAM heritage and the capabilities of the latest-generation Timepix series chips, we discuss their applicability for use in a compact magnetic spectrometer for a deep space mission or in the Jupiter radiation belts, as well as their capability for use as single-layer X- and  $\gamma$ -ray polarimeters. The latter was supported by the measurement of the polarization of scattered radiation in a laboratory experiment, where a modulation of 80% was found.

**Keywords:** space weather; scatter polarimeter; hybrid pixel detectors; Timepix; dE/dX spectrometer; low earth orbit; magnetic spectrometer; galactic cosmic rays; space instrumentation



**Citation:** Bergmann, B.; Gohl, S.; Garvey, D.; Jelínek, J.; Smolyanskiy, P. Results and Perspectives of Timepix Detectors in Space—From Radiation Monitoring in Low Earth Orbit to Astroparticle Physics. *Instruments* **2024**, *8*, 17. <https://doi.org/10.3390/instruments8010017>

Academic Editor: Pasquale Arpaia

Received: 30 October 2023

Revised: 12 February 2024

Accepted: 23 February 2024

Published: 29 February 2024



**Copyright:** © 2024 by the authors. Licensee MDPI, Basel, Switzerland. This article is an open access article distributed under the terms and conditions of the Creative Commons Attribution (CC BY) license (<https://creativecommons.org/licenses/by/4.0/>).

## 1. Introduction

In 1997, the Medipix collaboration was founded to evaluate hybrid pixel detector (HPD) technology, which was originally developed for particle tracking in high-energy physics for X-ray imaging [1]. Thus, single-photon-counting chips were developed, providing per-pixel information about the number of hits above predefined thresholds within a given time interval. Being mostly focused on the medical sector, these chips were called “Medipix”. In 2006, within the Medipix2 collaboration and upon the request of the EUDET collaboration, the first Timepix was released. It does not only determine the number of hits above a threshold, but it could also be set to measure the time from the moment of triggering the pixel to the end of the acquisition, thereby enabling a measurement of electron drift times released by ionizing radiation in gaseous volumes for resolving particle trajectories in 3D [2–4]. In addition, Timepix provides per-pixel spectroscopy using the time over threshold mode. The success of early Medipix and Timepix chips then triggered follow-up collaborations that further improved the technology by adding features to the pixel–signal processing, e.g., analog charge summing modes and additional thresholds or an improved time resolution and a data-driven readout architecture for the Medipix and Timepix series, respectively [5]. In addition to their rich application potential on Earth [5,6], Timepix detectors [7,8] have become increasingly interesting for radiation monitoring in space science.

To date, most of the commonly used space radiation monitors rely on silicon diodes, thereby achieving particle (mainly electron and proton) separation through pulse height analysis, detector stacking, shielding, or electron removal by a magnetic field. The key advantage of HPDs is that in addition to the energy deposition measurement, particle signatures in the sensor are seen as tracks with a rich set of features. These track characteristics can be exploited for the identification of particle type, energy, and its trajectory. Determining these pieces of information on a single layer bypasses the need for sensor stacking or complex shielding geometries, so that HPD-based space radiation devices provide science-class data with a large field of view at an order of magnitude of lower weight and approximately half of the power consumption compared to commonly used space radiation monitors or science-class energetic particle detectors.

Since 2012, Timepix has been utilized in radiation environment monitors aboard the ISS [9–11], being the first Timepix ( $256 \times 256$  pixels,  $55 \mu\text{m}$  pitch) used in open space is SATRAM (Space Application of Timepix Radiation Monitor) [12]. It is attached to the Proba-V, a satellite which was launched to low Earth orbit (LEO, 820 km, sun-synchronous orbit) in 2013 and has celebrated 10 years in orbit in May of 2023. During this time, it has been providing data for mapping out the fluxes of electrons and protons trapped in the Van Allen radiation belt, e.g., by in-orbit maps of the ionizing dose rate [13–15]. Over the years, different data analysis techniques have been successfully used for evaluation of the complex data set, including analytic categorization relying on the extraction of manually defined track features, as well as novel machine learning approaches [15–17]. The success of SATRAM initiated the development of advanced miniaturized space radiation monitors based on Timepix3 [18] and Timepix2 [19] technology. These are currently flown on the SWIMMR-1 (Space Weather Instrumentation, Measurement, Modelling and Risk) [20] mission (launched in 2023) and shall be used within the European Radiation Sensor Array (ERSA) [21].

The detector technology's science reach has been extended towards astroparticle physics application through the development of large area Timepix3 detectors ( $512 \times 512$  pixels,  $55 \mu\text{m}$  pitch) for the demonstrator of the penetrating particle analyzer [22] (Mini.PAN), which is a compact magnetic spectrometer (MS) designed to measure the properties of cosmic rays in the  $100 \text{ MeV}/n$ – $20 \text{ GeV}/n$  energy range in deep space with unprecedented accuracy, thus providing novel results to investigate the mechanisms of origin, acceleration, and propagation of galactic cosmic rays and of solar energetic particles, as well as producing unique information for solar system exploration missions.

Nanosecond-precision-per-pixel time measurement provided by state-of-the-art Timepix detectors, together with a high spatial granularity, makes it possible to resolve the drift times not only in gaseous volumes, as originally intended, but also in thin semiconductor sensors, thereby segmenting their detection volume into a 3D grid of voxels with the dimensions  $\sim(55 \times 55 \times 60) \mu\text{m}^3$  [23,24]. While the 3D reconstruction of interactions in the sensors improves the particle separation capability and impact angle determination, it also provides the means of using the detectors as a single-layer Compton camera for direction-sensitive hard X- or  $\gamma$ -ray detection [25–27]. The availability of sensors of different nuclear charge (e.g., silicon, CdTe/CZT, or GaAs) and thickness ( $\sim 100 \mu\text{m}$  to 5 mm) allows for the optimization of detection efficiency and the ratio of Compton and photopeak signal across a broad energy band, thereby making it worthwhile to evaluate the capabilities of Timepix as baseline or complementary detectors in missions dedicated to the study of sources of hard X-rays or  $\gamma$ -rays in the not yet well-explored energy range from 0.1–2 MeV, which constitutes the low energy part of the so-called “MeV gap” [28]. Additionally, the inherent sensitivity of the Compton camera to photon polarization [29] provides a handle to advance the understanding of astrophysical  $\gamma$ -ray sources and environmental conditions [30].

The present manuscript elaborates on the capabilities of Timepix-type detectors in the space environment. We will describe the already well-established use as a single-layer radiation detector in near Earth orbits using the example of SATRAM while outlining

their application potential as a tracker module in a compact magnetic spectrometer or as a compact Compton camera for direction- and polarization-sensitive X- and  $\gamma$ -ray detection.

## 2. Materials and Methods

### 2.1. Timepix Series

Among the different readout ASICs developed in the Medipix collaborations, the Timepix series, namely the Timepix [7], Timepix2 [19], Timepix3 [8], and Timepix4 [31] ASICs, were dedicated to single-particle detection and tracking:

- Timepix was developed within the Medipix2 collaboration [32]. It segments the sensor into a square matrix of  $256 \times 256$  pixels with a pixel pitch of  $55 \mu\text{m}$  and purely relies on a frame-based readout scheme (dead-time  $> 11$  ms). Each of the 65,536 pixels can be set to either of the three modes of signal processing: time-over-threshold (ToT), time-of-arrival (ToA, resolution  $> 10$  ns), and hit counting.
- Timepix2, while still relying on the frame-based readout, provides additional features, e.g., a simultaneous measurement of ToA and ToT and an adaptive gain ToT mode for improved spectroscopy at high-energy deposition [33].
- The key improvements of Timepix3 are a time resolution below 2 ns and the data-driven mode. The latter provides an almost dead-time-free detector operation by reading out only the pixels, which are actually triggered by an ionizing particle, while all other pixels remain active (per-pixel dead time:  $\sim 475$  ns). Pixel hit rates up to  $80 \text{ MHits s}^{-1}$  can be sent off a chip at a bandwidth of 5.12 Gbps.
- Timepix4 comes with an increased pixel matrix featuring  $512 \times 448$  pixels with a pitch of  $55 \mu\text{m}$  (resulting in an area of  $\sim 7 \text{ cm}^2$ ) [31]. Similar to Timepix3, it offers frame-based and data-driven readout schemes, but with  $8 \times$  higher maximal hit rate. The time binning is improved to 195 ps. The readout bandwidth can be up to 164 Gbps.

The ASICs can be coupled to different sensor materials by means of flip chip bump bonding. Currently available and tested sensor materials include silicon, CdTe, CZT, and high-resistivity chromium compensated GaAs:Cr with thicknesses ranging from  $100 \mu\text{m}$  to 2 mm. Improvements in growth techniques facilitate the availability of thick sensors with low defect density (CdTe, CZT, and GaAs:Cr), which profit from a higher  $\gamma$ -ray detection efficiency and single-layer tracking performance.

### 2.2. The Space Application of Timepix Radiation Monitor (SATRAM)

The first application of a Timepix in open space was SATRAM (Space Application of Timepix Radiation Monitor) onboard the Proba-V satellite (see Figure 1) launched in May 2013. The satellite is orbiting Earth in a Sun-synchronous orbit at an altitude of 820 km with an inclination of  $98.7^\circ$ . The orbit duration is 101.21 min, and the local time at descending node is between 10:30 a.m. and 11:30 a.m. The SATRAM module is encapsulated in an aluminium alloy compartment. It has a thinned area above the sensor with a thickness of 0.5 mm. The module weighs 380 g, has a power consumption of 2.5 W, and dimensions of  $55.5 \times 62.1 \times 197.1$  mm. The Timepix inside the module hosts a  $300 \mu\text{m}$  thick silicon sensor. The threshold is globally set to 8 keV. The detector is operated in the ToT mode, with acquisition times for consecutive frames set to 20 s, 200 ms, and 2 ms to account for the different flux levels in orbit.

SATRAM's continued operation allowed for measurements of fluxes of electrons and protons trapped in the Van Allen radiation belts continuously during its ongoing mission. Current proton and electron separation relies on pattern recognition, together with the  $dE/dX$  information. Recent work started to use convolution neural networks (CNNs) to improve classification accuracy [16]. Based on the success of SATRAM, proposals to develop a miniaturized radiation monitor (MIRAM) [18] and a highly integrated Timepix-based radiation monitor (HITPix) have been funded by the European Space Agency (ESA). The major differences that set these detectors apart from other commonly used radiation monitors like ICARE [34,35] or the Standard Radiation Environment Monitor (SREM [36,37]

are single-layer particle discrimination capabilities, which allow for the development of radiation monitors of small dimensions and low mass providing a large field of view.

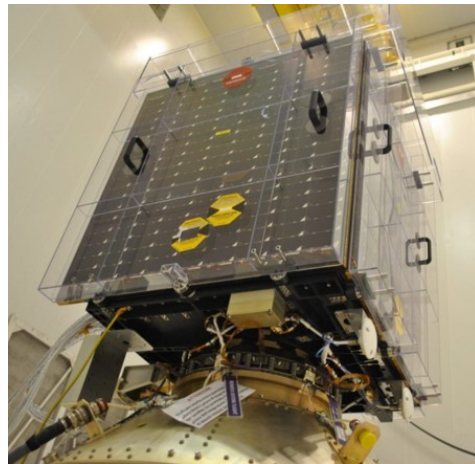


**Figure 1.** Picture of SATRAM attached to Proba-V.

### 2.3. Pattern Recognition Tools and Particle Separation

Detectors of the Timepix family are sensitive to a broad variety of particle species: from X-rays and electrons with energies just above 3 keV up to particles in the GeV range. Due to detector segmentation and the charge transport properties of the semiconductor sensors, ionizing particles create imprints in the pixel screen (clusters or tracks), which are to some extent usable for particle identification.

A basic pattern recognition scheme was introduced in 2008 [38]. It defines six categories of events: dots, small blobs, curly tracks, heavy blobs, heavy tracks, and straight tracks, with each indicating different particle species and energy depositions (Figure 2). This methodology purely relies on the track morphology. Additionally, Timepix allows for the use of the energy information, with which properties like the deposited energy, cluster height (the energy of the highest energy pixel in a cluster), and the stopping power can be determined. Timepix can also provide timing information, but not while simultaneously measuring the energy. This ability was added in subsequent generations with Timepix2 and Timepix3. Together with increased energy resolution, the particle recognition capability was thus improved.

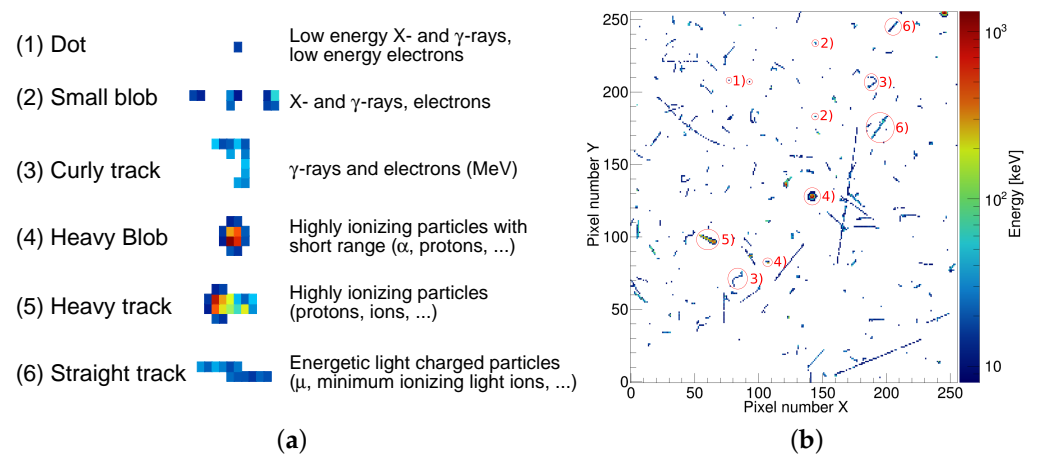


**Figure 2.** (a) Illustration of the cluster shape classification scheme proposed by [38]. (b) A 20 s frame of the SATRAM response to the radiation field as measured in space. The different shapes seen in the pixel matrix can be categorized, and exemplary tracks are labeled according to the scheme in (a).

A first attempt to identify particle species in the open space radiation environment with Timepix technology is presented in [14] using SATRAM data. In low Earth orbit, electrons and protons are the most abundant particle species. In there, the track properties used for particle separation are the above-mentioned track morphology, cluster height, and stopping power ( $dE/dx$ ). Monte Carlo simulations showed that for electrons, the cluster height is not higher than 300 keV, and the stopping power is not more than  $10 \text{ MeV cm}^2/\text{g}$ . The simulations were done for spectra that are expected in the radiation belts, i.e., for electrons with energies up to 7 MeV and protons with energies up to 400 MeV. While able to accurately determine electrons (correct classification in 98%), this method falls short in the identification of protons. High energy protons ( $>100 \text{ MeV}$ ) have a significant lower energy deposition and stopping power, which is on par with electrons. This is especially true for protons that pass through the detector perpendicularly, which create only short tracks that would often be misidentified as electrons.

In a follow-up work, neural networks were employed to improve previously achieved particle separation capability [16]. A fast Monte Carlo simulation of the detector response was used for the training of a CNN. Neglecting charge carrier transport, signal induction, and the behavior of the detector front end in the simulation, all particle tracks were only one pixel in width. While this is a valid approximation for the electron signatures, proton tracks seen in test beam measurements and in space data are usually two to four pixels wide. Still, it was shown that neural networks can be successfully used for particle identification in the case of electron- and proton-dominated space radiation data. Additionally, it was shown that the incident proton energy can be extracted, in particular at lower energy.

After implementing an improved detector response model accounting for charge sharing and induction to the previously used Monte Carlo simulation tool, another iteration of the NN was developed [15]. This feedforward neural network created in the TensorFlow framework [39] uses seven features to classify a cluster:

- The number of pixels in the cluster  $N$ ;
- The deposited energy  $E_{dep}$  is defined as the sum of energies measured in each pixel of a cluster  $E_{dep} = \sum_i^N E_i$ ;
- The maximal energy measured in a single pixel of the cluster  $E_{max} = \max\{E_0, \dots, E_N\}$ ;
- The linearity of the cluster, which is defined as the relative amount of pixel lying within a distance of one pixel from the longest line segment between two pixels of the cluster;
- The roundness of the cluster;
- The average number of neighboring pixels;
- The sum of the absolute values of cubic and quadratic terms of a third-order polynomial fit of the cluster.

The NN consists of an input layer, two hidden layers with seven neurons each, and one output layer. An overall testing accuracy of 90.2% was achieved, with protons being correctly classified in 89% and electrons in 91% of cases. In orbit, proton fluxes are still difficult to determine accurately, given that electron fluxes are often higher by about two orders of magnitude and electrons falsely identified as protons are of the same order of magnitude as the protons.

For the NN to work properly, it is required that clusters are well separated from each other. However, particle tracks inevitably overlap when frames have longer acquisition times and/or the fluxes are high. The NN is not able to recognize two or more tracks, let alone identify what particle species they are. To quantify this effect, occupancy has been introduced. It is calculated by the number of hit pixels divided by the number of available pixels. The result is expressed in percent. To ensure that the NN can work properly, only frames with a maximum occupancy of 20% were selected (low occupancy frames). For frames with higher occupancy (high occupancy frames), a different method had to be applied.

To estimate the electron fluxes of high occupancy frames, a statistical approach was chosen. The first step was to determine the mean energy of all clusters depending on the geographical position of the current measurement. The information was obtained by looking at the low occupancy frames in the region and calculating the mean energy for all particle tracks that were measured within the area. Typically, this local mean energy is higher in the SAA than the rest of the orbit due to the abundance of protons in that region. The estimation of the number of particles in the frame was then obtained by dividing the total measured energy in the frame by the local mean energy corresponding to the position of the satellite and then multiplying this by the fraction of electrons known from the previous low occupancy frame. Both methods are explained in detail in [15].

#### 2.4. $dE/dX$ Spectrum Unfolding

Spectrum deconvolution refers to the decomposition of a complex signal into its contributing spectrum components. There are many different iterative and statistical schemes that can be chosen for this process. In the present work, Bayesian unfolding has been chosen [40], which utilizes the probability formula:

$$p(A|B) = \frac{p(B|A)p(A)}{p(B)} \quad (1)$$

where  $p$  represents a generic probability function,  $|$  is the given operator, and  $A$  and  $B$  are some arbitrary variables or system states. Despite the simplicity of the Bayesian formula, it is quite powerful and used in many areas of physics and statistics. The formula conveys the probability of  $A$  having a particular value or state given that  $B$  has a particular value or state, thereby essentially relating two otherwise unrelated states. The states  $A$  and  $B$  can be assigned some arbitrary distribution of two variables that will be referred to as the cause vector ( $x_C$ ) and the effect vector ( $x_E$ ), respectively. It can then be assumed that there exists an arbitrary probability distribution  $p(x_E|x_C)$  given by the formula

$$p(x_C|x_E) = \frac{p(x_E|x_C)p(x_C)}{p(x_E)}. \quad (2)$$

The approximate values of  $p(x_E|x_C)$  can be achieved through simulation. The remaining probability values for a specific experiment can be obtained through the Bayesian iterative deconvolution algorithm that is implemented using the library [41].

To use the Bayesian deconvolution algorithm, an incoming spectrum ( $x_C$ ) is related to the measured spectrum ( $x_E$ ) in a so-called “response matrix”. Since previous works [42,43] have demonstrated the sensitivity of the  $dE/dX$  measurement to incident proton kinetic energy, we have chosen a response matrix relating the  $dE/dX$  spectra to an incoming monoenergetic omnidirectional electron or proton field (Figure 3). For each detected track, the stopping power was calculated as:

$$\frac{dE}{dX} = \frac{\sum_{i=0}^N E_i}{t_{\text{sensor}} \times \rho_{\text{Si}} \times \cos \theta} \quad (3)$$

with the per-pixel energy of a particle trace being  $E_i$ , the sensor thickness being  $t_{\text{sensor}} = 300 \mu\text{m}$ , the density of silicon being  $\rho_{\text{Si}} = 2.33 \text{ g cm}^{-3}$ , and the reconstructed impact angle with respect to the sensor normal being  $\theta$ .

Accounting for expected particles and energies, the response spectra were simulated in  $N_e$  electron primary energy bins and  $N_p$  proton primary energy bins with a flat distribution from 0 to 6 MeV and 0 to 400 MeV, respectively, using an in-house developed simulation tool based on Geant4 [44]. An omnidirectional particle environment was approximated by emitting  $N_{\text{sim}} = 3 \times 10^6$  protons and  $2 \times 10^6$  electrons with a  $\cos^2(\theta)$  initial momentum direction distribution from the surface of a spherical source with a radius of  $R_{\text{source}} = 20 \text{ cm}$ . In order to speed up the simulation, and since we are only interested in particles arriving at

the sensor, the emission angle range was restricted to point towards the sensor or its close surroundings, i.e.,  $\theta \in [0, 3]$  degree.

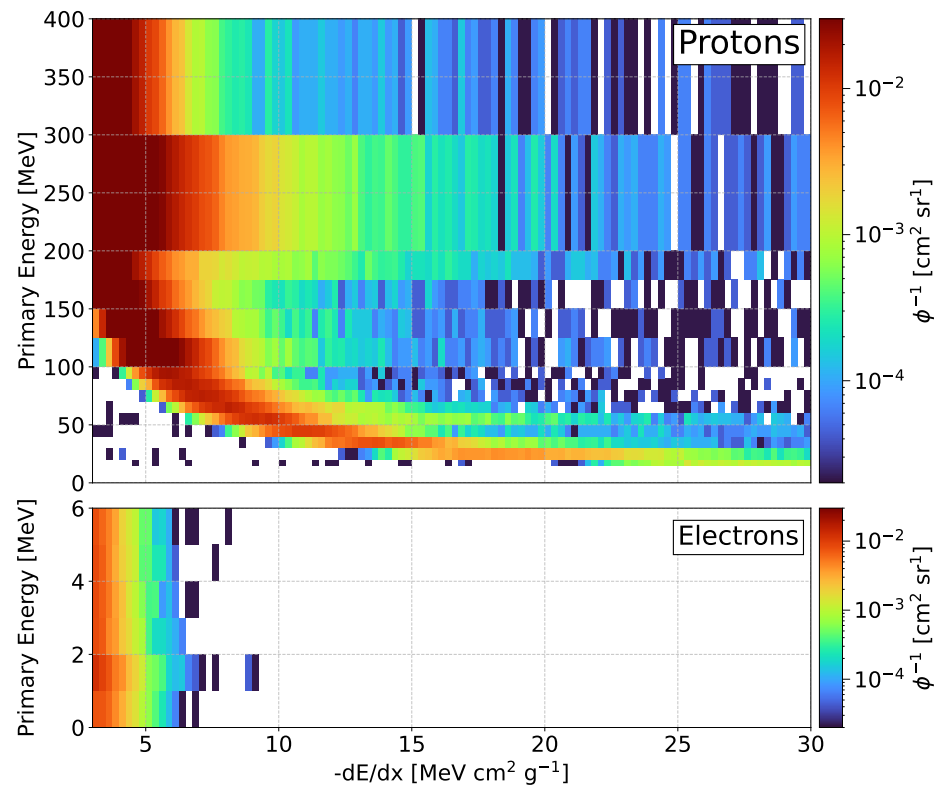


**Figure 3.** Graphical visualization of the response matrix ( $p(x_C|x_E)$ ) used for the Bayesian deconvolution approach described in the text. It was obtained through simulation.

The response matrix was scaled with the particle flux through the sensitive volume, which was calculated for the simulated geometry as:

$$\frac{d\Phi_{\text{sim}}}{dA d\Omega} = \frac{N_{\text{sim}}}{A_{\text{surface}} \Omega_{\text{emission}}}, \quad (4)$$

$$\text{with } A_{\text{surface}} = 4\pi R_{\text{source}}^2 \quad (5)$$

$$\text{and } \Omega_{\text{emission}} = \int_0^{2\pi} d\varphi \int_0^{\frac{\pi}{60}} \cos(\theta) \sin(\theta) d\theta = \frac{1}{2} \left[ 1 - \cos\left(\frac{\pi}{60}\right) \right]. \quad (6)$$

The response matrix obtained likewise is presented in Figure 3. Asymmetric binning was chosen for the  $y$  axis to reflect the varying sensitivity towards spectral changes, which is higher at high stopping power (slow protons) and lower for higher energy protons. It can be seen that all electrons  $\geq 1$  MeV were degenerate and all protons were asymptotically electron-like with increasing energy.

The presented methodology has been validated in clinical monoenergetic proton beams at the Danish Center for Particle Therapy, thereby finding proper incident energy reconstruction with angle-averaged incident energy resolutions of  $\sigma_{125\text{MeV}} = 17$  MeV,  $\sigma_{175\text{MeV}} = 28$  MeV, and  $\sigma_{225\text{MeV}} = 42$  MeV at beam energies of 125 MeV, 175 MeV, and 225 MeV, respectively [45].

### 2.5. 3D Reconstruction of Particle Traces within the Semiconductor Sensor—Use as a Solid State Time Projection Chamber

Ionizing radiation interacting in the sensors creates free charge carriers, which start to drift towards the electrode of opposing charge. During this drift motion, currents are induced at the pixels in close vicinity. Due to the small pixel size compared to sensor

thickness, detectable signals are only induced if the charge carriers are close to the pixel side (small pixel effect) so that the measured time corresponds approximately to the drift time across the sensor thickness.

The charge carrier (electrons  $e$  and holes  $h$ ) drift along the  $z$  axis of the device can be described by

$$\vec{v}_e = -\mu_e \times \vec{E} \tag{7}$$

$$\vec{v}_h = \mu_h \times \vec{E} \tag{8}$$

where  $\mu_{e/h}$  is the mobility of electron and holes, respectively. For planar silicon sensors in hole collection, a linear parameterization of the electric field can be used (see e.g., [23]):

$$\vec{E} = \frac{U_B}{d} \vec{e}_z + \frac{2U_{dep}}{d^2} \times \left( \frac{d}{2} - z \right) \vec{e}_z, \tag{9}$$

where  $d$  denotes the sensor thickness,  $U_B$  is the bias voltage, and  $U_{dep}$  is the depletion voltage. While  $U_{dep}$  depends on the quality of the sensor and should be determined individually, we can use  $U_{dep} = 40 \text{ V} \times \left( \frac{d}{300 \mu\text{m}} \right)^2$  as a rule of thumb. For semi-insulation planar sensors (CdTe, CZT, and GaAs:Cr) with ohmic contacts, we assume a linear electric field across the sensor thickness:

$$\vec{E} = \frac{U_B}{d} \vec{e}_z. \tag{10}$$

While the charge carrier drift motion can be described analytically, the induction process requires numeric calculation (iterative simulation). Therefore, the charge carrier drift motion and the amount of deposited charges were modeled, thereby creating lookup tables relating the energy deposition and measured time stamps to the interaction depth (see [24]).

The methodology was applied to silicon and CdTe sensors of thickness  $500 \mu\text{m}$  [23] and  $2 \text{ mm}$  [24], respectively, thus finding  $z$  resolutions of  $\sim 30 \mu\text{m}$  and  $60 \mu\text{m}$ , respectively. Figure 4 shows typical event displays of 3D-reconstructed particle trajectories measured in relativistic particle beams.

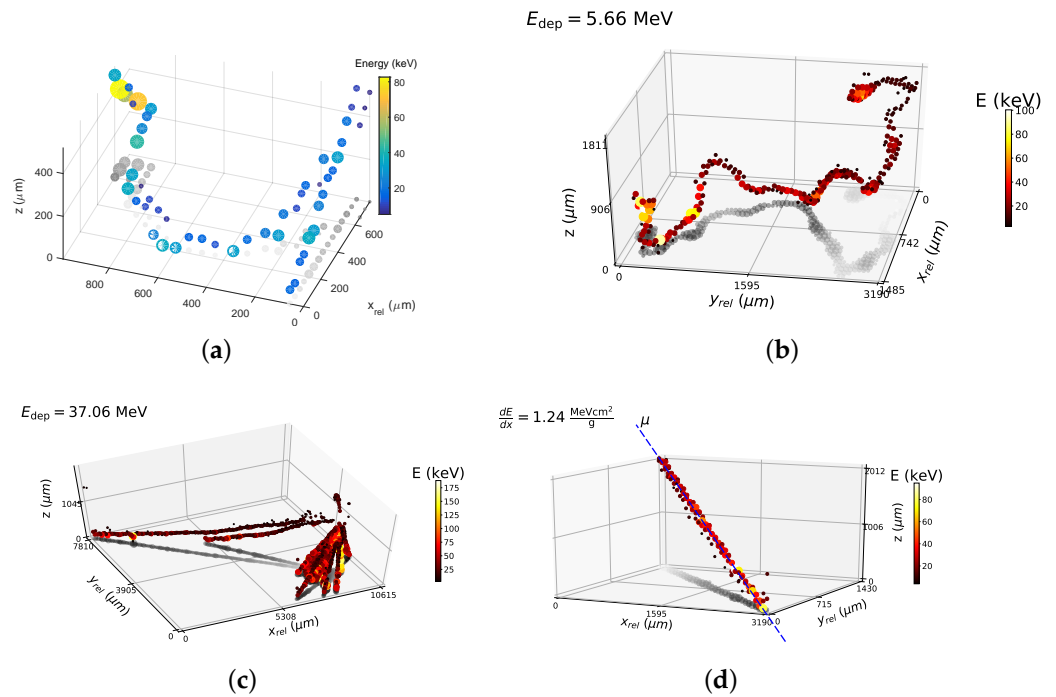


**Figure 4.** Event displays of 3D reconstructions of tracks: (a) 120 GeV/c pion passing through a 500  $\mu\text{m}$  thick silicon sensor; (b,c) high-energy electron and fragmentation reaction measured during exposure

of a 2 mm thick CdTe sensor to a 180 GeV/c pion beam; (d) cosmic muon with a 3D line fit. Fitting the trajectory allows for a trajectory reconstruction with precision of  $<200 \mu\text{m}$  evaluated at a distance of 1 m. Reproduced from [23,24] (CC BY 4.0, no changes were made).

## 2.6. Single-Layer Compton Camera and Scatter Polarimetry

Fine pixelation and the (above-described) 3D reconstruction within the sensor permit Timepix3 utilization as a single-layer Compton camera. For this purpose, the Compton electron has to be detected together with the scattered X-ray photoelectron. With the Compton electron detected at  $\vec{r}_e$  depositing energy  $E_e$  and the scattered photon detected at  $\vec{r}'_\gamma$  with energy  $E'_\gamma$ , we can define Compton cones around the axis defined by the directional vector  $\vec{r}_{\text{dir}} = \vec{r}'_\gamma - \vec{r}_e$  with tips located at  $\vec{r}_e$  [25]. The opening angle is given by

$$\cos \beta = 1 - m_e c^2 \times \left( \frac{1}{E'_\gamma} - \frac{1}{E_\gamma} \right) \quad (11)$$

with  $m_e c^2 = 511 \text{ keV}$  being the electron rest energy, and  $E_\gamma = E_e + E'_\gamma$  [25].

Polarized incoming radiation will create an asymmetry in the scattering angles evaluated, which can be described by the Klein–Nishina formula [29]

$$\frac{d\sigma}{d\Omega} = \frac{r_e^2}{2} \left( \frac{E'_\gamma}{E_\gamma} \right)^2 \left( \frac{E'_\gamma}{E_\gamma} + \frac{E_\gamma}{E'_\gamma} - 2 \sin^2(\beta) \cos^2(\varphi - \varphi_0) \right) \quad (12)$$

where  $r_e = 2.818 \times 10^{-15} \text{ m}$  is the classical radius of an electron,  $\beta$  is the angle of the outgoing photon with respect to the direction of the incoming photon, and  $\varphi - \varphi_0$  is the angle between the scattering plane and polarization plane. The scattered photon preferentially flies perpendicularly ( $\|\varphi_{\text{pref}} - \varphi_0\| = 90^\circ \implies \cos^2(\varphi_{\text{pref}} - \varphi_0) = 0$ ) to the polarization of the incoming photon.

Concurrent detection of the Compton electron with the photoelectron therefore allows for the assessment of the X-ray polarization. Without loss of generality, we take the detector's  $x$  axis as reference and determine the angle  $\varphi$  as  $\cos \varphi = \vec{r}_{\text{dir}} \cdot \vec{e}_x / |\vec{r}_{\text{dir}}|$ , where  $\vec{e}_x$  is the  $x$  axis unit vector. For partially polarized photon impact, the scattering angles  $\varphi$  will be distributed as

$$f(\varphi) = A(\mu \cos(2(\varphi - \varphi_0)) + 1), \quad (13)$$

where  $A$  is a scaling factor,  $\mu$  is the modulation, and the phase  $\varphi_0$  determines the polarization direction of the incoming X-rays with respect to the  $x$  axis. Here, we assumed that our detector is equally sensitive in all azimuthal directions  $\varphi$ . The degree of polarization is then

$$P = \frac{\mu}{\mu_{100}}, \quad (14)$$

where  $\mu_{100}$  denotes the modulation response to a 100% polarized X-ray impact, which can be calibrated in simulation [46] or in a field of known polarization.

## 3. Results

### 3.1. Space Heritage—SATRAM and Its 10 Years of Operation as a Radiation Monitor

#### 3.1.1. Measurement Stability—Noisy Pixel Appearance and Removal

In this section, the state of SATRAM in terms of radiation-induced effects on data quality shall be quantified. This will be done by looking at the amount of noisy pixels that may occur over time in a different quantity. Noisy pixels are defined as pixels exceeding the overall count rate at a statistically significant level. While most of the identified noisy pixels were recoverable and disappeared after resetting the detector configuration, some became permanently noisy. The latter were masked (removed from the data set) and, thus, are not

considered in the analysis. Given that there are 65,536 pixels, the loss of a few hundred pixels is negligible for the overall data quality.

To determine if a pixel is noisy, one usually takes an arbitrarily high number of frames and counts how often a each pixel has sent a signal. In this study, the noisy pixel search was performed on the timescale of one week. The number of counts measured in each of the pixels within this time period were registered in a histogram. The resulting distribution was then fitted with a Gaussian distribution, therein obtaining the mean  $N_{\text{mean}}$  and the standard deviation  $\sigma$ . We defined the threshold for a pixel to be considered as noisy,  $N_{\text{max}}$ , as

$$N_{\text{max}} = N_{\text{mean}} + 5 \times \sigma. \quad (15)$$

This procedure was done for every consecutive week from the beginning of available data in August 2014 until the 30 June 2023. Furthermore, this analysis was performed separately for the three different acquisition times. Naturally, more pixels will have sent a signal in longer frames than in shorter ones, which could have skewed the distributions. The resulting relative numbers of noisy pixels are shown in Figure 5.

Until the end of 2021, the number of noisy pixels were below 0.6%. In 2021, there were two periods, in spring and autumn, where an increased amount of noisy pixels was present over a few weeks. The same can be seen for the year 2022, but with a significantly higher number of noisy pixels. No definite explanation has been found for the increase nor for the periodicity.

In 2023, the detector seemed to have recovered. A careful inspection of the data has shown that most of the data was measured as expected. There were a few cases where the matrix became filled up to a large portion while being in the corresponding region of space where no high fluxes of radiation were expected. While the statistical method for noisy pixel determination used here is not suitable to detect this kind of behavior, these frames stood out and were excluded from analysis by comparison of their count rates with previous and subsequent frames.

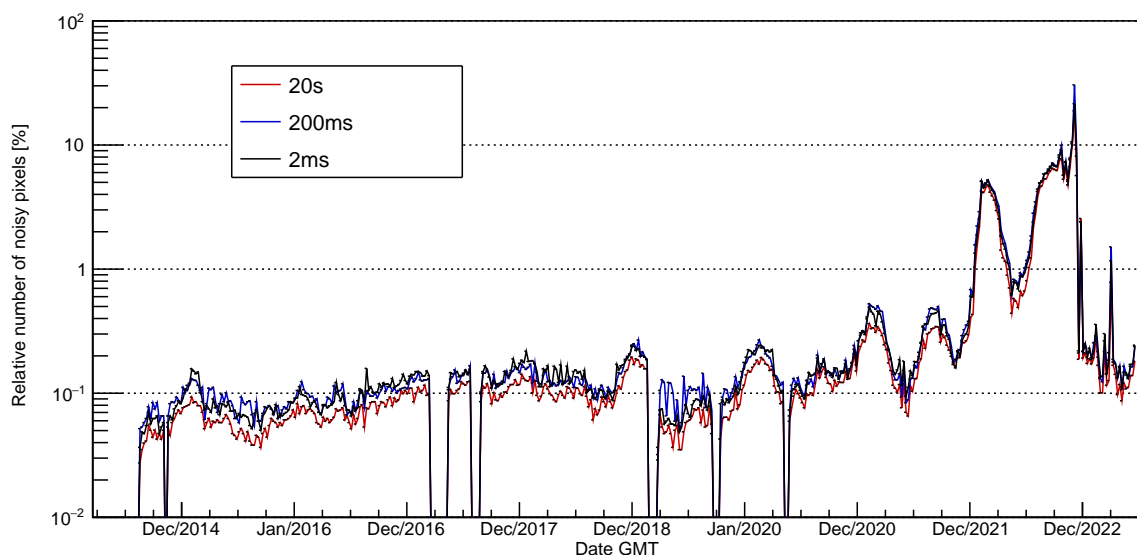


**Figure 5.** Relative number of pixel classified as noisy on a weekly basis from August 2014 to the end of June 2023 for the Timepix in SATRAM. The number of noisy pixels stayed below 0.6% until the end of 2021. In 2022, numbers were rising with a maximum of about 22% near the end of the year. The detector recovered in 2023.

The distribution of noisy pixels over the pixel matrix for the years 2015 and 2022 can be seen in Figure 6a and 6b, respectively. In 2015, most noisy pixels were concentrated in the lower left corner. This is a well-known firmware issue of SATRAM and was present already from the beginning. These pixels have been excluded from analysis in all previous

studies. In 2022, the pixels in the lower left corner were still noisy and seemed to have worsened. Additionally, pixels along the edge were showing increased noise behavior. The edge pixels being noisy can be observed in many frames acquired in 2022. However, their position makes it easy to mask them and eliminate them from analysis. Their exclusion resulted in a reduction in the usable detector area by 21%.

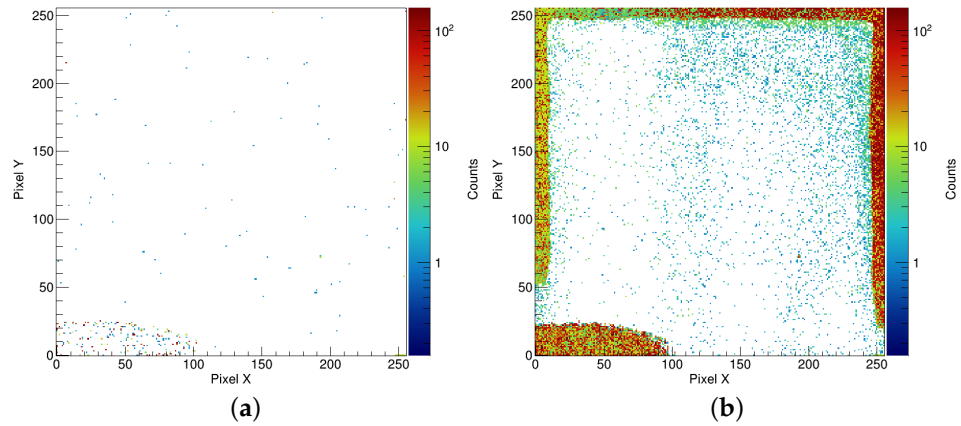


**Figure 6.** Noisy pixel distribution over the Timepix sensor for the years 2015 (a) and 2022 (b). The pixels in the lower left corner were damaged during launch of the Proba-V satellite. The color bar represents how often the pixels were considered noisy on a weekly basis and across all three acquisition times.

A follow up analysis, using the same method for noisy pixel detection but for a reduced number of pixels, was performed. The noisy pixels in the lower left corner and the edge pixels as seen in Figure 6b have been masked (excluded). The result is presented in Figure 7. The number of noisy pixels was greatly reduced to below 0.2%, except for a short period in late 2022, where about 10% of pixels were identified as noisy. This shows that by restricting the active area of the sensor through masking the problematic areas, SATRAM provides reasonable data during its entire 10 years of operation.

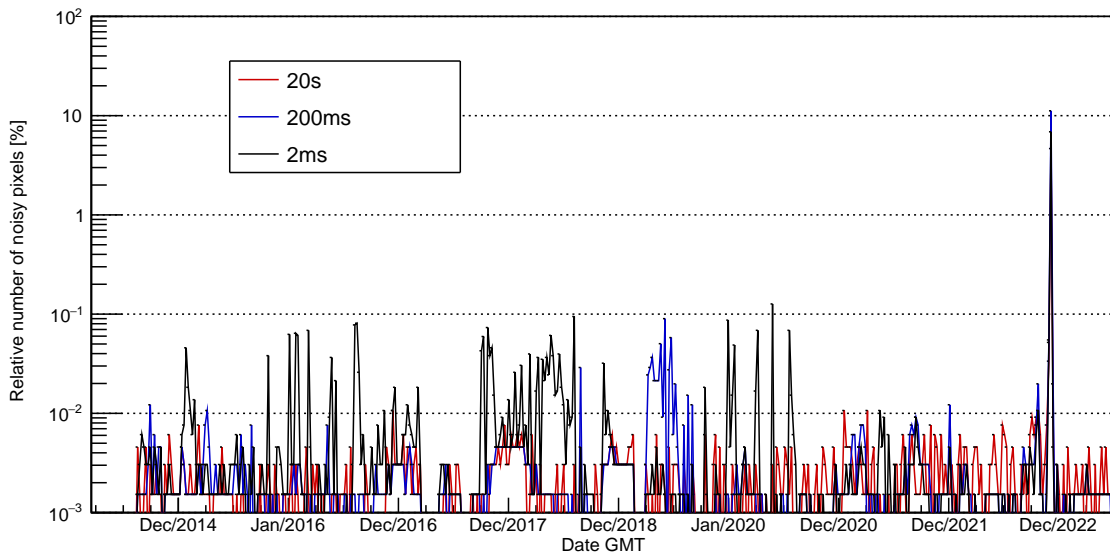


**Figure 7.** Same as Figure 5, but excluding noisy pixels from the lower left corner and pixels on the edges of the sensor, as seen in Figure 6b. The number of noisy pixels is greatly reduced.

### 3.1.2. Mapping Out Electron and Proton Fluxes in Orbit

Figure 8a,b show the fluxes of electrons and protons classified with the method described in Section 2.3. The majority of particles present in the radiation environment in LEO were protons (up to 400 MeV) and electrons (up to 7 MeV) that were trapped by the Earth's magnetic field. For electrons, three distinct structures are discernible, i.e., the northern polar horn, the southern polar horn, and the South Atlantic Anomaly (SAA). The northern and southern polar horns correspond to the points at which the satellite passed through the Earth's outer radiation belt. The SAA is present due to the satellite crossing the Earth's inner radiation belt. This crossing is possible due to the incline of the Earth's magnetic dipole combined with the deviation of the Earth's magnetic center with respect to the Earth's center of mass. While the outer radiation belt consists of electrons, the SAA is the only area in SATRAM's orbit, where a non-negligible flux of protons should be present. Thus, protons seen in the polar horns (in Figure 8b) were interpreted as misclassified electrons.

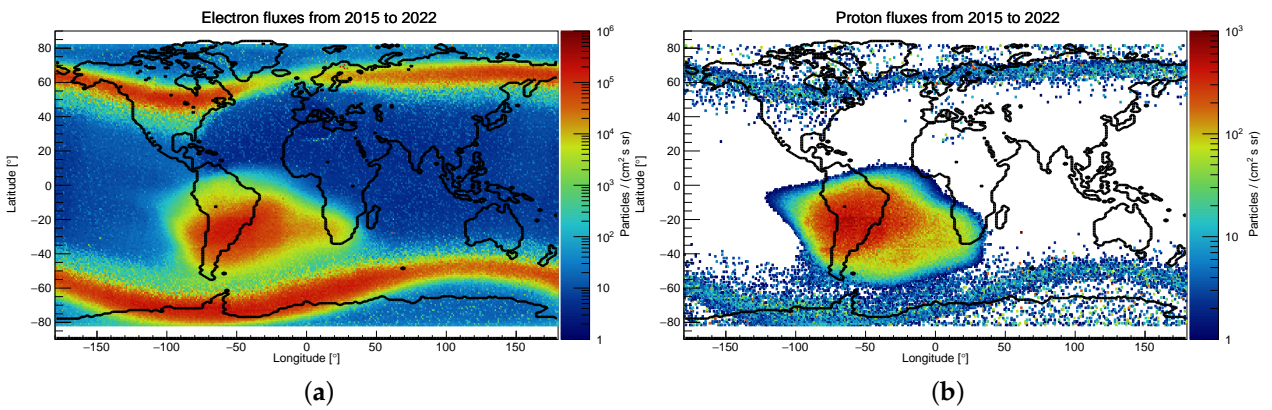


**Figure 8.** Electron (a) and proton (b) flux rates as measured with SATRAM at 820 km altitude in low Earth orbit averaged over the years from 2015–2022.

### 3.1.3. Measurement of the Proton Spectrum in the SAA

Figure 9a shows the  $dE/dX$  spectrum reconstructed for the central region of the SAA defined by  $longitude \in [-70^\circ, -25^\circ]$  and  $latitude \in [-40^\circ, -12^\circ]$ . To avoid track overlap, which could result in an improper  $dE/dX$  determination, only tracks measured within the shortest frames (2 ms acquisition time) were used for the analysis. Within such frames, the matrix occupancy was consistently below 10%. A total of 22,784 frames were found during 2015–2018 operation, thus giving in a total effective measurement time of  $t_{meas.} = 45.568$  s.

By applying the unfolding methodology defined in Section 2.4 to the measured  $dE/dX$  spectrum, we obtain the spectral-resolved differential flux equation:

$$\Phi_{tot}^{unfold.}(E) = \frac{N}{\Delta E d\Omega dt dA'} \quad (16)$$

where  $N$  denotes the number of particles measured within a bin of width  $\Delta E$  per unit solid angle  $d\Omega$ , area  $dA$ , and time  $dt$ . It is shown as the blue curve in Figure 9b. Since no prior selection of the particle signature was performed,  $\Phi_{total}^{unfold.}$  was thus defined as a linear combination of the differential proton ( $p$ ) and electron ( $e$ ) fluxes:

$$\Phi_{total}^{unfold.}(E) = \Phi_p^{unfold.}(E) + \Phi_e^{unfold.}(E). \quad (17)$$

As shown in Figure 3, the  $dE/dX$  response to the electrons is incident energy spectrum independent. We can thus estimate the “electron background” by applying Bayesian unfolding to the  $dE/dX$  spectrum simulated with an arbitrary incident electron energy spectrum. Thus, for our convenience, we utilized the simulation results of the above-described response matrix determination. In this way, we obtained an unfolded simulated

fluence  $\Phi_{\text{sim.}}^{\text{unfold.}}$ , which is of proper spectral shape, but still needs to be scaled to resemble the electron flux rate from the measurement. This was accomplished using the relation

$$\Phi_e^{\text{unfold.}}(E) = \frac{N_e^{\text{meas.}}/dt}{N_e^{\text{sim.}}} \times \Phi_{\text{sim.}}^{\text{unfold.}}, \quad (18)$$

where  $N_e^{\text{meas.}}/dt$  is the flux rate of particles identified as electrons in the measurement, and  $N_e^{\text{meas.}}$  denotes the number of electrons detected in the simulation. The electron contribution obtained in this way is depicted in Figure 9b (in orange color). It becomes visible for the energy region above  $\sim 100$  MeV and dominates the count rate above  $\sim 140$  MeV.

The differential proton flux  $\Phi_p^{\text{unfold.}}$  was then obtained by binwise subtraction of  $\Phi_{\text{total}}^{\text{unfold.}}$  and  $\Phi_e^{\text{unfold.}}$ . An additional 20% error was added to account for possible systematic errors due to inaccurate detector response modeling. In Figure 9c, the result of the present work is compared with proton spectra measured with the EPT at different locations within the SAA [47]. Four geographic bins were close to the center, and a fifth bin was located at the edge of the SAA. While the overall spectral shapes of the EPT fell steeper with energy than the ones of the SATRAM, the deviations evaluated at each measured point were on a one sigma level over the entire energy range and across different locations. Considering that the data of the EPT and SATRAM were taken at different times, that the SATRAM bin averages the spectrum over a significantly larger geographic region, and the fact that the EPT has a limited field of view becoming narrower with higher proton energy, the agreement of our results with the EPT data is satisfactory.

### 3.2. Large Area Timepix3 Detectors as Tracking Modules in a Magnetic Spectrometer

The development of a penetrating particle analyzer (Mini.PAN) started in January 2020 in a collaboration formed by the Department of Nuclear and Particle Physics at the University of Geneva, the National Institute of Nuclear Physics at the Perugia Section, and the Institute of Experimental and Applied Physics of the Czech Technical University. Mini.PAN employs position-sensitive (pixel and strip) detectors and (fast) scintillators to infer the particle type and velocity of GeV particles (and antiparticles) passing through the instrument's magnetic field by measuring their bending angles, charge deposition, and time of flight. Once in orbit, this device allows for a precise measurement of flux, composition, spectral characteristics, and directions of penetrating cosmic rays over the full solar cycle, thereby inherently providing the capability to search for antimatter. While such measurements exist within the heliosphere, Mini.PAN is designed as a compact instrument with low mass operating at low power. Thus, it could be used in deep space or on smaller satellites. Figure 10a shows the developed pixel module featuring four Timepix3 detectors in a  $2 \times 2$  geometry (quad) giving a  $7.92 \text{ cm}^2$  area with 262,144 pixels at a pixel pitch of  $55 \mu\text{m}$ . Figure 10 shows the pixel module integrated into the demonstrator.

Figure 11 shows the stopping power spectra measured with the developed device at different angles within a relativistic hadron beam (90% pions) measured at the CERN SPS. The distributions are modeled as the convolution of a Landau curve describing the physics the particle energy loss in the sensor smeared with a Gaussian whose width indicates the detector's energy resolution. Rotation of the device allows for the study of this resolution at different deposited energy. We find  $\sigma(83.2 \text{ keV}) = 4.1 \text{ keV}$  (5%),  $\sigma(97.1 \text{ keV}) = 6.4 \text{ keV}$  (6.6%), and  $\sigma(180 \text{ keV}) = 13 \text{ keV}$  (7.2%).

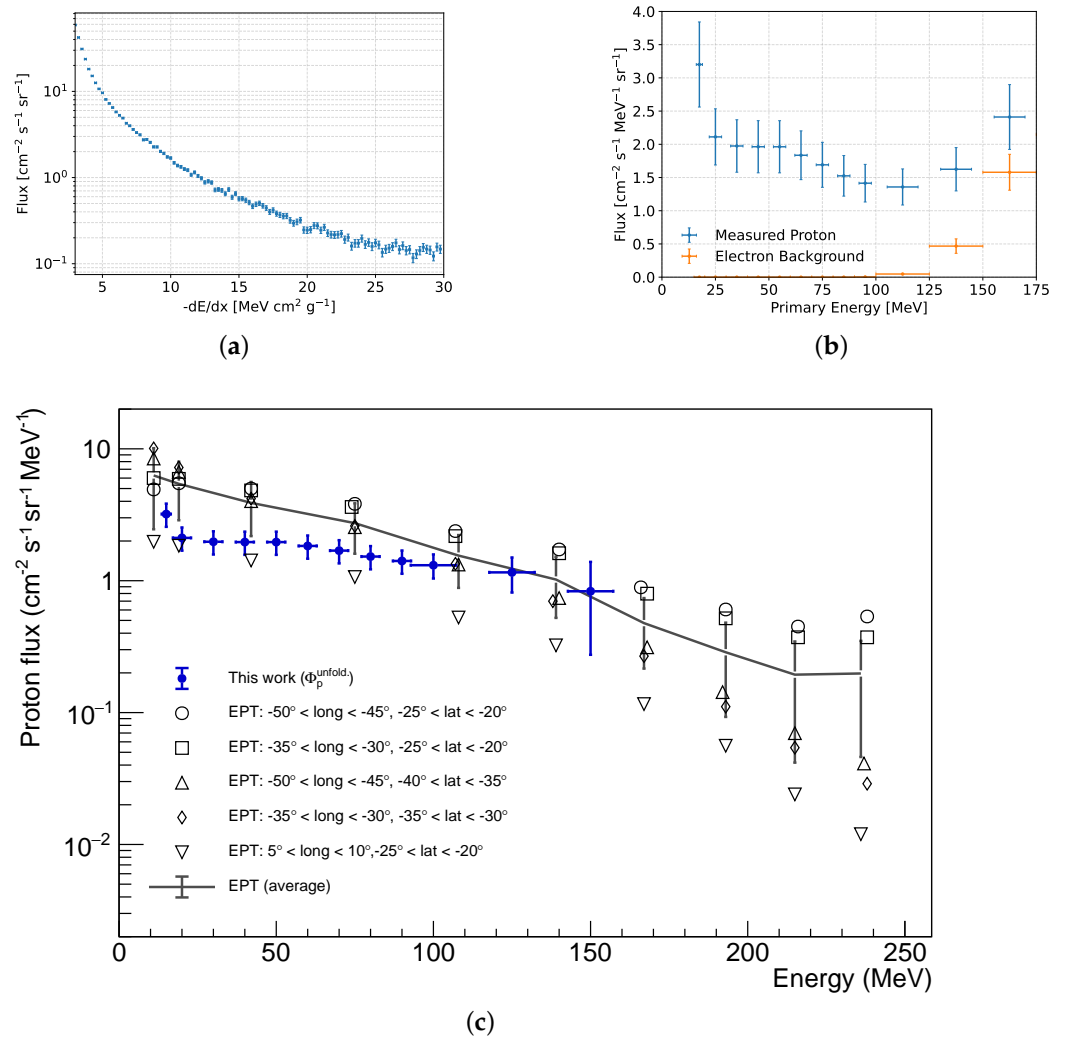


**Figure 9.** (a)  $dE/dX$  spectrum measured in the SAA used as input for the unfolding methodology. (b) Results of the unfolding methodology described in Section 2.4 for the  $dE/dX$  spectrum of (a) (blue line). The electron contribution determined in simulation (orange line, see text for details). (c) The energy-dispersive differential proton flux after electron background subtraction (blue markers). The SATRAM data measured within the SAA bin ( $longitude \in [-70^\circ, -25^\circ]$ ,  $latitude \in [-40^\circ, -12^\circ]$ ) are compared with a previous analysis of the EPT team [47] measuring at different geographic locations (different markers). The solid line resembles the average of these measurement points. Since the errors for the different locations are the same, these are drawn representatively for the averaged flux for improved visualization.

A detailed study of the temperature influence on the device performance and different operational parameters providing low power operation have been presented [48]. In the best case, a power consumption of  $\sim 2$  W for the entire quad was achievable.

### 3.3. Capabilities of Timepix3 as a Compton Camera and Scatter Polarimeter

The capabilities of a single-layer Timepix3 for use as a Compton polarimeter was studied in a laboratory experiment. The experimental setup is shown in Figure 12a. X-rays from a Hamamatsu microfocus tube were collimated onto a relatively large plastic target (dimensions:  $2 \times 2 \times 2$  cm<sup>3</sup>) placed at a distance of 21.5 cm to the collimator. The tube voltage was set at  $U_{\text{tube}} = 75$  kV with a tube current of  $I_{\text{tube}} = 60$   $\mu$ A. A 1 mm thick pixelated silicon sensor (55  $\mu$ m pixel pitch) attached to Timepix3, reverse biased at 400 V, was used to detect the scattered X-rays.

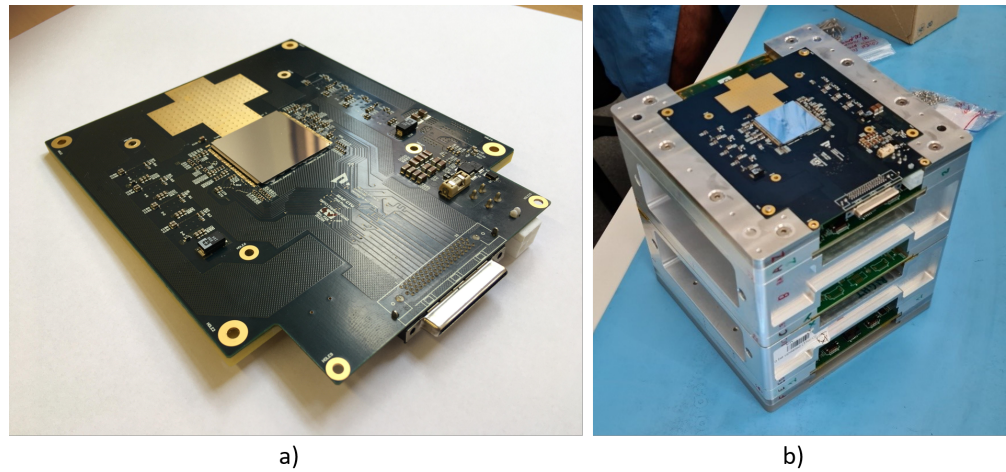


**Figure 10.** (a) Picture of the Timepix3  $2 \times 2$  module developed for the use in demonstrator of a penetrating particle analyzer; (b) Timepix3 quad integrated into the Mini.PAN front end.

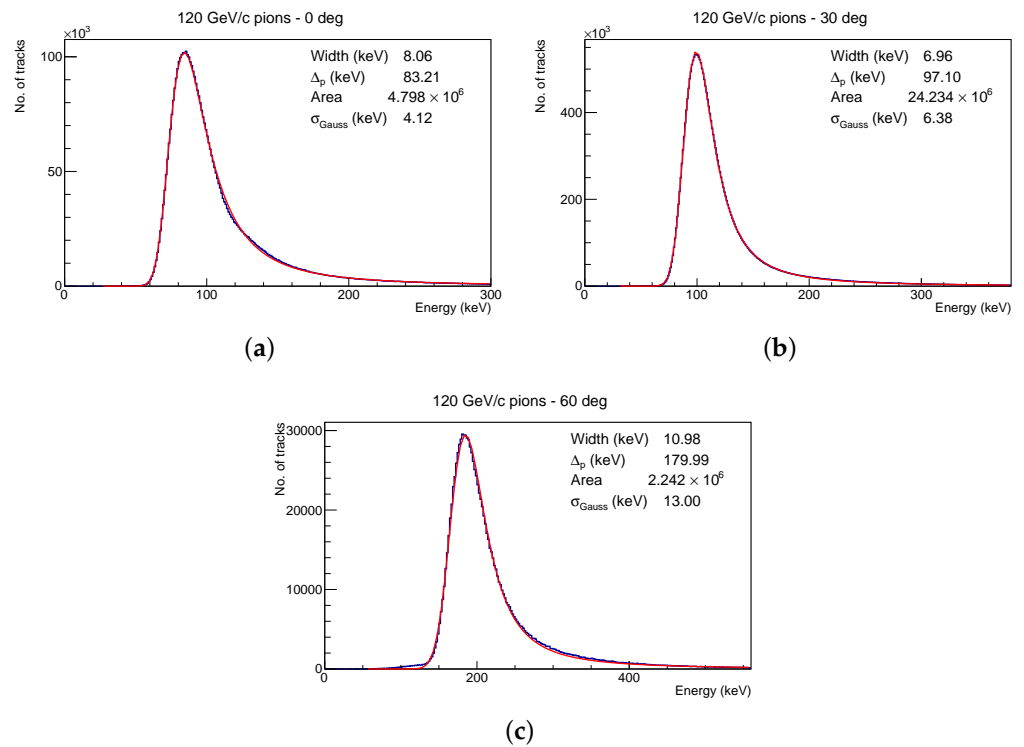


**Figure 11.** Energy deposition spectra measured with the Timepix3 quad module in a 180 GeV/c pion beam fitted with a Landau curve convolved with a Gaussian: (a) at perpendicular particle impact; (b) at 30 degrees; and (c) at 60 degrees impact angle with respect to the sensor normal.

The detector was placed at 16 cm from the target in a way that the X-rays of the highest degree of polarization (scattering off the target at  $90^\circ$ ) could be recorded. Using the detector in data-driven operation, we searched for coincidentally detected pairs of clusters using a floating time window of  $\Delta t = 65$  ns (drift time of holes across the whole thickness of the sensor). We refer to a set of coincidentally detected clusters as a “coincidence group”. Coincidence groups larger than two clusters were omitted from the analysis. The cluster with higher energy  $E'_\gamma$  in each coincidence pair was assumed to be a photoelectron deposited by the scattered photon, while the lower energies  $E_e$  were assigned to Compton electrons. The histogram of energies of the clusters within coincident groups is shown in Figure 12b separately for clusters labeled as Compton electrons and as photoelectrons. The

incoming photon energy was reconstructed by summing the two energy measurements  $E_\gamma = E'_\gamma + E_e$ . Using Equation (11), we calculated cosine of the scattering and selected only pairs with  $-1 \leq \cos \beta \leq 1$ .

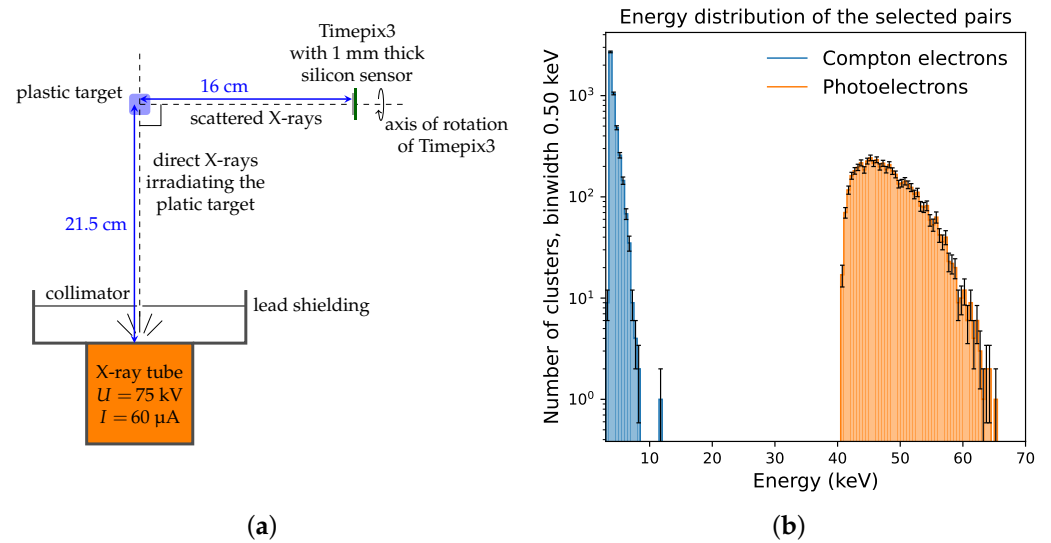


**Figure 12.** (a) Experiment design: A collimated beam from a Hamamatsu microfocus X-ray tube hits a plastic target to create polarized X-rays, which are absorbed in a 1 mm thick Timepix3 detector. The detector was placed at  $90^\circ$  to the axis defined by the tube and scattering target. A tube voltage  $U_{\text{tube}} = 75 \text{ kV}$  was used at the tube current  $I_{\text{tube}} = 60 \text{ }\mu\text{A}$ . (b) Energy histogram of the selected pairs of clusters. Compton scattering clusters with energies  $\lesssim 3.5 \text{ keV}$  could not be detected due to per pixel detection threshold.

We further applied a cut on the pixel plane distance between the coincident clusters  $d = \sqrt{\Delta x^2 + \Delta y^2}$ , thereby restricting the range to  $1.0 \text{ mm} < d < 10.0 \text{ mm}$ . Figure 13 shows the measured scattering angle distributions fitted with Equation (13) to determine the modulation  $\mu$  and phase shift  $\varphi_0$ . Overall, a modulation of 80% was found. To demonstrate that the seen modulation was in fact an effect observable in the laboratory frame and not inherent to the technology, the detector was rotated around the axis defined by the target and detector. The observed phase shifts  $\varphi_0$  were consistent with the angle offsets.

Figure 14 shows the Compton camera reconstruction using simple back projection. Relative 3D coordinates were calculated as described in Section 2.5 using the timestamp measured by the Compton cluster within the coincidence pair as the time reference ( $t_{\text{ref}}$ ). Furthermore, each cone was assigned a weight that favored cluster pairs with a higher energy of Compton electrons  $E_e$  (less uncertainty in  $\cos \beta$ ), a larger absolute time of arrival difference  $\|\Delta t\|$  (being close to either 0.0 ns or 65 ns), and a greater distance  $d$  (less uncertainty in cone axis vector).

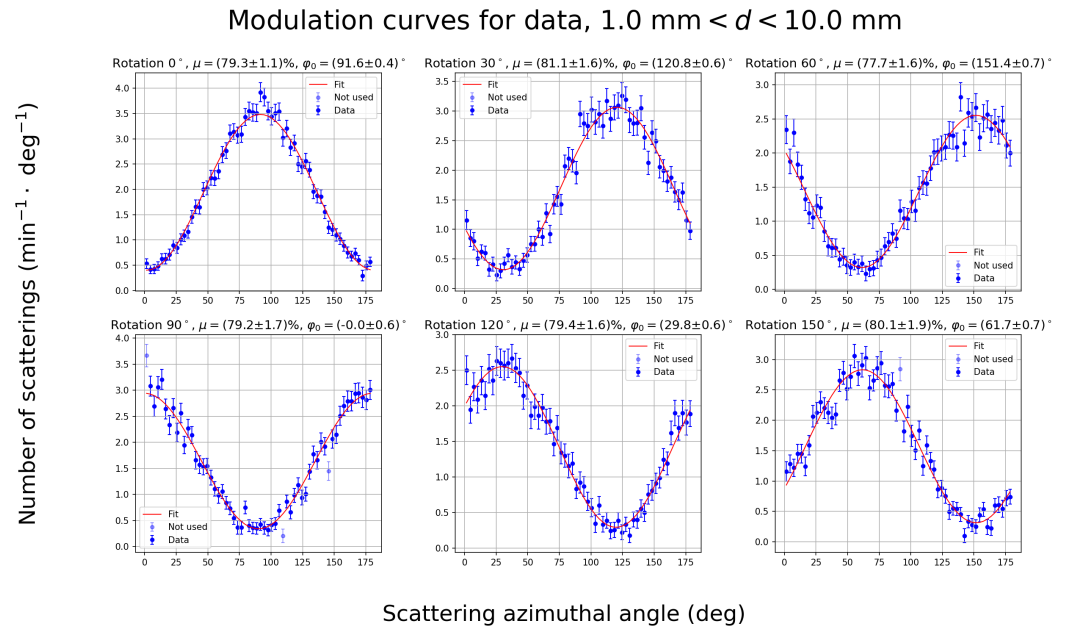


**Figure 13.** Modulations measured within the detector plane presented at different angles around the axis defined by the target and detector.

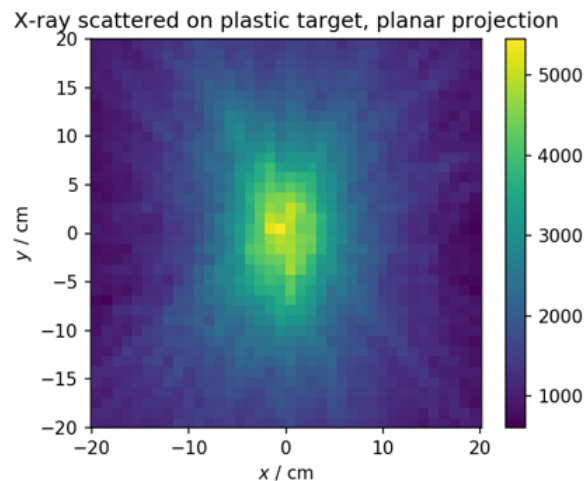


**Figure 14.** Application of the single-layer Compton camera reconstruction to the measured data.

## 4. Discussion

### 4.1. Timepix-Based Radiation Monitors

In contrast to commonly used space radiation monitors, Timepix-based devices provide the capability to separate different particle classes with a single-layer detector. This allows for the development of competitive low mass ( $\sim 100 \text{ g}$ ) radiation detectors, which inherently provide an almost  $4\pi$  field of view. In the present contribution, we have outlined these capabilities through the example of SATRAM, which has been operated in open space for more than 10 years.

While Timepix can be considered as a noise-free individual particle detector, due to single-event effects appearing in chip registers, individual pixels can “lose” their configuration and become noisy until their configuration is reset. Long-term irradiation additionally results in electronics baseline shifts, which could affect the noise behavior of the entire sensor. We have studied the appearance of noise patterns in the measured data by searching for outlier pixels with unphysically high count rates. For the first 8 years of operation, the number of such pixels was consistently on the level of 0.6%. During 2022 operation, the number of noisy pixels reached values of up to 22% and recovered in 2023. It was found

that the noise level increase in particular affected pixels at the edges of the sensor, which were subsequently excluded to reduce the relative amount of noisy pixels to 0.1% (with the exception of a short period in late 2022 with up to 10%). While the effectively used detector area had to be reduced by 21% for 2022 operation, the overall data quality and scientific reach of the detector was not affected.

The current limitation of SATRAM compared to, e.g., with the Energetic Particle Telescope, is its insensitivity to resolve the spectral characteristics of incoming radiation. Within in the present work, we have overcome this problem—at least for protons—using a novel spectrum unfolding methodology. For the first time, we were able to present a proton energy spectrum measured with a single-layer device in low Earth orbit. The obtained result is consistent with a previous measurement performed with the science-class instrument EPT [47]. A comprehensive discussion and comparison with state-of-the-art radiation belt models like AP-8 [49] or AP-9 [50] is out of the scope of this work. Energy-selective detection of electrons in the LEO radiation environment still remains unsolved, and should be addressed in future development, e.g., by implementing multidetector devices with sensors of differing stopping power or by adding electron stopping filters to the backside of the sensor.

A drawback of Timepix is that measurements are taken in frames of predefined acquisition times. Thus, at changing radiation fluxes, the overexposure of frames can occur and lead to track overlap and the misclassification of events. The typical mitigation strategy is the adjustment of frame times with the consecutive selection of frames with acceptable occupancy for analysis. While adaptive techniques for frame time adjustment are presented in [10], a computationally inexpensive approach had to be chosen for SATRAM. Measurements were collected in a predefined sequence of frames with acquisition times of 20 s, 0.2 s, and 2 ms. The overexposure issue has been addressed with the design of next generation Timepix ASICs. For example, Timepix2 provides “online” monitoring of the frame occupancy with automatic frame termination once a preset amount of columns is triggered; Timepix3 implements a data-driven mode, where only pixels triggered by radiation are read out, while all others remain active. The latter, however, comes with the possibility of high measured data rates. Considering typically limited resources for data storage and downlink, this imposes the requirement for an onboard data compression. Therefore, methodology and algorithms are needed that can analyze the data at low computing power. Development going in this direction has been started.

#### 4.2. Towards Astroparticle Physics Application

Highly spatially segmented detectors with decent time resolutions are also a valuable asset for astroparticle physics instrumentation. In contrast to the space weather and radiation dosimetry studies, where small detectors are beneficial, astrophysical observations usually require detectors of a large area to cope with low flux rates.

##### 4.2.1. From Mini.PAN to Pix.PAN

A Timepix3 quad detector was developed for application in Mini.PAN, which is a two-sector magnetic spectrometer proposed for an in situ spectrum-resolved measurement of the galactic cosmic ray fluxes. The developed detectors have an effective area of  $7.92 \text{ cm}^2$ , segmented in 262.144 pixels of  $55 \times 55 \mu\text{m}^2$ . In the current instrument design, they are mainly supplemental detectors adding high flux capabilities, an additional charge, and position measurement. Their limited spatial ( $dx = 55/\sqrt{12} \mu\text{m} = 16 \mu\text{m}$ ) and temporal resolution ( $\sim 2 \text{ ns}$ ), prevents them from being used as a standalone tracker (requirement:  $dx < 7 \mu\text{m}$ ) or as a segmented time-of-flight module (requirement:  $dt < 200 \text{ ps}$ ). As outlined in [51], these issues can be overcome by the latest generation of Timepix-series chips, Timepix4, thus inherently providing a time granularity of  $< 200 \text{ ps}$  combined with an adapted sensor design using a “pitch adapter” to create rectangular pixels of  $13.75 \times 1760 \mu\text{m}^2$  in area. The small pitch in bending direction is sufficient for measuring the curvature of particles in the range up to  $10 \text{ GeV}/c$  with the baseline Mini.PAN Halbach magnets of  $0.5 \text{ T}$  [22]. The

lax requirement in the nonbending direction further makes it possible to save power by switching off 7/8 of the pixels. The production and testing of the novel sensor design has been started.

The Pix.PAN design relies on three tracking stations, with each consisting of a stack of two Timepix4 quads [51]. While the synchronization of 24 detectors at picosecond precision requires careful electronics design, relying on a single detector technology represents a significant simplification compared to Mini.PAN. The high-rate capability of Timepix4 will allow for application in harsh radiation environments, such as the Jovian radiation belts.

#### 4.2.2. Compton Scatter Polarimetry

At last, we have presented a simple laboratory experiment demonstrating the capability of Timepix3 to be used as a single-layer Compton camera and scatter polarimeter. Therefore, we profited from the capability of reconstructing the locations of the interaction of ionizing radiation within thick sensors in 3D, which was enabled by nanosecond-scale drift time measurement. We measured the modulation for X-rays from a microfocus tube (tube voltage: 75 kV) scattered at 90 degrees in a plastic target to be  $\mu_{\text{meas.}} = 80\%$ . This represented an improvement of  $\sim 29\%$  compared to previous work [46] using Timepix in a similar experiment (finding a modulation of 62%).

To further understand the detectors capability, a simulation in Geant4 [44] with X-rays hitting a  $14.08 \times 14.08 \times 1.0 \text{ mm}^3$  silicon sensor was carried out. Simulated X-ray beams were monoenergetic, nondispersive, had a uniform spatial distribution, and were arriving at an angle of  $90^\circ$  to the sensor plane. Three types of beams were simulated: unpolarized, 100% polarized with polarization direction at  $0^\circ$ , and 100% polarized with the polarization vector oriented at  $30^\circ$  to to the sensor's  $x$  axis. Only events with the photon interacting twice in the sensor were selected. The same cuts on  $\cos \beta$  and distance  $d$  were made as for the experimental data. Interactions with an energy deposit  $E_{\text{dep}} < 3.5 \text{ keV}$ , resembling the per pixel energy threshold, were omitted. We found that for 100% polarization in the incoming photon energy range from 45 to 75 keV, a modulation  $\mu_{100} > 92\%$  could be achieved. We can assess the performance of the device according to the minimum detectable polarization (MDP) at a 99% confidence level describing the degree of linear polarization detectable within a given acquisition time. Neglecting the background, it can be estimated as [46]

$$\text{MDP}_{99\%} = \frac{4.29}{\mu_{100} \times \sqrt{N_{\text{det}}}}, \quad (19)$$

where  $N_{\text{det}}$  is the number of detected scatter electron–photon pairs, and  $\mu_{100}$  is the modulation measured at 100% polarized radiation. We can solve Equation (19) for  $N_{\text{det}}$  to estimate the minimal amount of detected scatter events:

$$N_{\text{det}} = \frac{4.29^2}{\mu_{100}^2 \times \text{MPD}_{99\%}^2}. \quad (20)$$

With  $\mu_{100} = 92\%$  (from the simulation) and  $\text{MPD}_{99\%} = 10\%$ , we find  $N_{\text{det}} = 2000$ . Further simulation studies implementing proper detector responses shall be the topic of future work and should focus on improving event selection criteria or obtaining ground truth data samples for machine learning techniques. The possibility to use different sensor materials of various thicknesses with the same Timepix readout ASIC hereby allows for the selection of sensors optimized for the desired photon energy range. The larger area and lower power density per unit area of Timepix4 will further enhance the applicability for space research. Thus, future work should study the capabilities of thick CdTe/CZT (studied up to 5 mm [52,53]) devices for measurement in the hard X-ray band, terrestrial  $\gamma$  flashes, or  $\gamma$ -ray bursts.

## 5. Conclusions

In summary, we have demonstrated that Timepix-family detectors' capability of single-layer particle tracking and particle species separation allows for the production of competitive radiation monitors with one order of reduction in mass and covering almost the entire solid angle range. The application of novel methodology utilizing the Timepix3 time resolution for the reconstruction of the  $z$  coordinate provides 3D reconstruction of particle tracks, which in "thick" sensors enables their use as a single-layer Compton camera and scatter polarimeter. Here, the possibility to combine the readout ASIC with sensors of different materials provides a means of optimization for different  $X$ - and  $\gamma$ -ray bands. While currently, Timepix3 detectors are an integral part of particle spectrometers for measurements of galactic cosmic ray properties (Mini.PAN), Timepix4 could be a baseline technology of future magnetic spectrometers, thereby adding high rate capability and electronics simplification (Pix.PAN).

**Author Contributions:** Conceptualization, B.B.; Formal analysis, D.G., S.G. and J.J.; Funding acquisition, B.B.; Investigation, J.J.; Methodology, B.B., S.G., D.G. and J.J.; Project administration, B.B.; Resources, P.S.; Software, S.G., D.G. and J.J.; Supervision, B.B. and S.G.; Validation, S.G., D.G. and J.J.; Visualization, S.G., D.G. and J.J.; Writing—original draft preparation, B.B.; Writing—review and editing, S.G., D.G., J.J. and P.S. All authors have read and agreed to the published version of the manuscript.

**Funding:** The authors B.B., D.G., and P.S. are grateful for the funding received by the Czech Science Foundation (GACR) under grant number GM23-04869M. The development of the Timepix3 Quad module for Mini.PAN was funded by the European Union's Horizon 2020 research and innovation programme under grant agreement No. 862044.

**Data Availability Statement:** All SATRAM data are available through the online tool <https://satram.utef.cvut.cz/> (accessed on 26 February 2024). Other presented data and the reconstruction codes used are available upon request.

**Acknowledgments:** Successful launch and operation of SATRAM would not have been possible without Stanislav Pospíšil, Carlos Granja, and Alan Owens.

**Conflicts of Interest:** The authors declare no conflicts of interest.

## Abbreviations

The following abbreviations are used in this manuscript:

ASIC	Application-Specific Integrated Circuit
CdTe	Cadmiumtelluride
CZT	Cadmiumzinctelluride
GaAs:Cr	Chromium-Compensated Galliumarsenide
CNN	Convolution Neural Network
ESA	European Space Agency
EPT	Energetic Particle Telescope
HITPix	Highly Integrated Timepix radiation monitor
HPD	Hybrid pixel detector
ICARE	Influence sur les Composants Avancés des Radiations de l'Espace
LEO	Low Earth Orbit
MIRAM	Miniaturized Radiation Monitor
MS	Magnetic Spectrometer
MPD	Minimum Detectable Polarization
NN	Neural Network
PAN	Penetrating Particle Analyzer
SAA	South Atlantic Anomaly
SATRAM	Space Application Timepix Radiation Monitor
SPENVIS	Space Environment Information System
SREM	Standard Radiation Environment Monitor
SWIMMR	Space Weather Instrumentation, Measurement, Modelling and Risk

## References

1. Campbell, M. 10 years of the Medipix2 Collaboration. *Nucl. Instruments Methods Phys. Res. Sect. A Accel. Spectrometers Detect. Assoc. Equip.* **2011**, *633*, S1–S10. [CrossRef]
2. Campbell, M.; Heijne, E.; Llopart, X.; Colas, P.; Giganon, A.; Giomataris, Y.; Chefdeville, M.; Colijn, A.; Fornaini, A.; van der Graaf, H.; et al. GOSSIP: A vertex detector combining a thin gas layer as signal generator with a CMOS readout pixel array. *Nucl. Instruments Methods Phys. Res. Sect. A Accel. Spectrometers Detect. Assoc. Equip.* **2006**, *560*, 131–134. [CrossRef]
3. Bamberger, A.; Desch, K.; Renz, U.; Titov, M.; Vlasov, N.; Wienemann, P.; Zwerger, A. Resolution studies on 5 GeV electron tracks observed with triple-GEM and MediPix2/TimePix-readout. *Nucl. Instruments Methods Phys. Res. Sect. A Accel. Spectrometers Detect. Assoc. Equip.* **2007**, *581*, 274–278. [CrossRef]
4. George, S.; Murtas, F.; Alozy, J.; Curioni, A.; Rosenfeld, A.; Silari, M. Particle tracking with a Timepix based triple GEM detector. *J. Instrum.* **2015**, *10*, P11003. [CrossRef]
5. Ballabriga, R.; Campbell, M.; Llopart, X. ASIC developments for radiation imaging applications: The medipix and timepix family. *Nucl. Instruments Methods Phys. Res. Sect. A Accel. Spectrometers Detect. Assoc. Equip.* **2018**, *878*, 10–23. [CrossRef]
6. Jakübek, J. Semiconductor Pixel detectors and their applications in life sciences. *J. Instrum.* **2009**, *4*, P03013. [CrossRef]
7. Llopart, X.; Ballabriga, R.; Campbell, M.; Tlustos, L.; Wong, W. Timepix, a 65k programmable pixel readout chip for arrival time, energy and/or photon counting measurements. *Nucl. Instruments Methods Phys. Res. Sect. A Accel. Spectrometers Detect. Assoc. Equip.* **2007**, *581*, 485–494. [CrossRef]
8. Poikela, T.; Plosila, J.; Westerlund, T.; Campbell, M.; De Gaspari, M.; Llopart, X.; Gromov, V.; Kluit, R.; Van Beuzekom, M.; Zappone, F.; et al. Timepix3: A 65K channel hybrid pixel readout chip with simultaneous ToA/ToT and sparse readout. *J. Instrum.* **2014**, *9*, C05013. [CrossRef]
9. Stoffle, N.; Pinsky, L.; Kroupa, M.; Hoang, S.; Idarraga, J.; Amberboy, C.; Rios, R.; Hauss, J.; Keller, J.; Bahadori, A.; et al. Timepix-based radiation environment monitor measurements aboard the International Space Station. *Nucl. Instruments Methods Phys. Res. Sect. A Accel. Spectrometers Detect. Assoc. Equip.* **2015**, *782*, 143–148. [CrossRef]
10. Kroupa, M.; Bahadori, A.; Campbell-Ricketts, T.; Empl, A.; Hoang, S.M.; Idarraga-Munoz, J.; Rios, R.; Semones, E.; Stoffle, N.; Tlustos, L.; et al. A semiconductor radiation imaging pixel detector for space radiation dosimetry. *Life Sci. Space Res.* **2015**, *6*, 69–78. [CrossRef] [PubMed]
11. Kroupa, M.; Campbell-Ricketts, T.; Bahadori, A.A.; Pal Chowdhury, R.; Empl, A.; George, S.P.; O'Brien, T.P. Extravehicular Electron Measurement Based on an Intravehicular Pixel Detector. *J. Geophys. Res. Space Phys.* **2019**, *124*, 8271–8279. [CrossRef]
12. Granja, C.; Polansky, S.; Vykydal, Z.; Pospisil, S.; Owens, A.; Kozacek, Z.; Mellab, K.; Simcak, M. The SATRAM Timepix spacecraft payload in open space on board the Proba-V satellite for wide range radiation monitoring in LEO orbit. *Planet. Space Sci.* **2016**, *125*, 114–129. [CrossRef]
13. Granja, C.; Polansky, S.; Vykydal, Z.; Pospisil, S.; Turecek, D.; Owens, A.; Mellab, K.; Nieminen, P.; Dvorak, Z.; Simcak, M.; et al. Quantum imaging monitoring and directional visualization of space radiation with timepix based SATRAM spacecraft payload in open space on board the ESA Proba-V satellite. In Proceedings of the 2014 IEEE Nuclear Science Symposium and Medical Imaging Conference (NSS/MIC), Seattle, WA, USA, 8–15 November 2014; pp. 1–2. [CrossRef]
14. Gohl, S.; Bergmann, B.; Evans, H.; Nieminen, P.; Owens, A.; Pospisil, S. Study of the radiation fields in LEO with the Space Application of Timepix Radiation Monitor (SATRAM). *Adv. Space Res.* **2019**, *63*, 1646–1660. [CrossRef]
15. Gohl, S.; Bergmann, B.; Kaplan, M.; Némec, F. Measurement of electron fluxes in a Low Earth Orbit with SATRAM and comparison to EPT data. *Adv. Space Res.* **2023**, *72*, 2362–2376. [CrossRef]
16. Ruffenach, M.; Bourdarie, S.; Bergmann, B.; Gohl, S.; Mekki, J.; Vaillé, J. A New Technique Based on Convolutional Neural Networks to Measure the Energy of Protons and Electrons With a Single Timepix Detector. *IEEE Trans. Nucl. Sci.* **2021**, *68*, 1746–1753. [CrossRef]
17. Furnell, W.; Shenoy, A.; Fox, E.; Hatfield, P. First results from the LUCID-Timepix spacecraft payload onboard the TechDemoSat-1 satellite in Low Earth Orbit. *Adv. Space Res.* **2019**, *63*, 1523–1540. [CrossRef]
18. Gohl, S.; Bergmann, B.; Pospisil, S. Design Study of a New Miniaturized Radiation Monitor Based on Previous Experience with the Space Application of the Timepix Radiation Monitor (SATRAM). In Proceedings of the 2018 IEEE Nuclear Science Symposium and Medical Imaging Conference Proceedings (NSS/MIC), Sydney, NSW, Australia, 10–17 November 2018; pp. 1–7. [CrossRef]
19. Wong, W.; Alozy, J.; Ballabriga, R.; Campbell, M.; Kremastiotis, I.; Llopart, X.; Poikela, T.; Sriskaran, V.; Tlustos, L.; Turecek, D. Introducing Timepix2, a frame-based pixel detector readout ASIC measuring energy deposition and arrival time. *Radiat. Meas.* **2020**, *131*, 106230. [CrossRef]
20. RAL Space SWIMMR-1. Available online: <https://www.ralspace.stfc.ac.uk/Pages/SWIMMR-1-launches-in-boost-to-UK-space-weather-forecasting-capabilities.aspx> (accessed on 26 October 2023).
21. Filgas, R. (Institute of Experimental and Applied Physics, Czech Technical University, Prague, Czechia). Private communication, 2023.
22. Wu, X.; Ambrosi, G.; Azzarello, P.; Bergmann, B.; Bertucci, B.; Cadoux, F.; Campbell, M.; Duranti, M.; Ionica, M.; Kole, M.; et al. Penetrating particle ANalyzer (PAN). *Adv. Space Res.* **2019**, *63*, 2672–2682. [CrossRef]
23. Bergmann, B.; Pichotka, M.; Pospisil, S.; Vycpalek, J.; Burian, P.; Broulim, P.; Jakubek, J. 3D track reconstruction capability of a silicon hybrid active pixel detector. *Eur. Phys. J. C* **2017**, *77*, 421. [CrossRef]

24. Bergmann, B.; Burian, P.; Manek, P.; Pospisil, S. 3D reconstruction of particle tracks in a 2 mm thick CdTe hybrid pixel detector. *Eur. Phys. J. C* **2019**, *79*, 165. [[CrossRef](#)]
25. Turecek, D.; Jakubek, J.; Trojanova, E.; Sefc, L. Single layer Compton camera based on Timepix3 technology. *J. Instrum.* **2020**, *15*, C01014. [[CrossRef](#)]
26. Amoyal, G.; Schoepff, V.; Carrel, F.; Michel, M.; Blanc de Lanaute, N.; Angélique, J. Development of a hybrid gamma camera based on Timepix3 for nuclear industry applications. *Nucl. Instruments Methods Phys. Res. Sect. A Accel. Spectrometers Detect. Assoc. Equip.* **2021**, *987*, 164838. [[CrossRef](#)]
27. Wen, J.; Zheng, X.; Gao, H.; Zeng, M.; Zhang, Y.; Yu, M.; Wu, Y.; Cang, J.; Ma, G.; Zhao, Z. Optimization of Timepix3-based conventional Compton camera using electron track algorithm. *Nucl. Instruments Methods Phys. Res. Sect. A Accel. Spectrometers Detect. Assoc. Equip.* **2022**, *1021*, 165954. [[CrossRef](#)]
28. Carena, P.; la Torre Luque, P.D. Detecting neutrino-boosted axion dark matter in the MeV gap. *Eur. Phys. J. C* **2023**, *83*. [[CrossRef](#)]
29. Caroli, E.; Moita, M.; Da Silva, R.M.C.; Del Sordo, S.; De Cesare, G.; Maia, J.M.; Páscoa, M. Hard X-ray and Soft Gamma Ray Polarimetry with CdTe/CZT Spectro-Imager. *Galaxies* **2018**, *6*, 69. [[CrossRef](#)]
30. Weisskopf, M.C. An Overview of X-Ray Polarimetry of Astronomical Sources. *Galaxies* **2018**, *6*, 33. [[CrossRef](#)]
31. Llopart, X.; Aloy, J.; Ballabriga, R.; Campbell, M.; Casanova, R.; Gromov, V.; Heijne, E.; Poikela, T.; Santin, E.; Sriskaran, V.; et al. Timepix4, a large area pixel detector readout chip which can be tiled on 4 sides providing sub-200 ps timestamp binning. *J. Instrum.* **2022**, *17*, C01044. [[CrossRef](#)]
32. Medipix Collaboration. Available online: <https://medipix.web.cern.ch/home> (accessed on 18 July 2023).
33. Bergmann, B.; Smolyanskiy, P.; Burian, P.; Pospisil, S. Experimental study of the adaptive gain feature for improved position-sensitive ion spectroscopy with Timepix2. *J. Instrum.* **2022**, *17*, C01025. [[CrossRef](#)]
34. Boscher, D.; Bourdarie, S.A.; Falguere, D.; Lazaro, D.; Bourdoux, P.; Baldran, T.; Rolland, G.; Lorfèvre, E.; Ecoffet, R. In Flight Measurements of Radiation Environment on Board the French Satellite JASON-2. *IEEE Trans. Nucl. Sci.* **2011**, *58*, 916–922. [[CrossRef](#)]
35. Boscher, D.; Cayton, T.; Maget, V.; Bourdarie, S.; Lazaro, D.; Baldran, T.; Bourdoux, P.; Lorfèvre, E.; Rolland, G.; Ecoffet, R. In-Flight Measurements of Radiation Environment on Board the Argentinean Satellite SAC-D. *IEEE Trans. Nucl. Sci.* **2014**, *61*, 3395–3400. [[CrossRef](#)]
36. Evans, H.; Bühler, P.; Hajdas, W.; Daly, E.; Nieminen, P.; Mohammadzadeh, A. Results from the ESA SREM monitors and comparison with existing radiation belt models. *Adv. Space Res.* **2008**, *42*, 1527–1537. [[CrossRef](#)]
37. Sandberg, I.; Daglis, I.A.; Anastasiadis, A.; Bühler, P.; Nieminen, P.; Evans, H. Unfolding and validation of SREM fluxes. In Proceedings of the 2011 12th European Conference on Radiation and Its Effects on Components and Systems, Seville, Spain 19–23 September 2011; pp. 599–606. [[CrossRef](#)]
38. Holy, T.; Heijne, E.; Jakubek, J.; Pospisil, S.; Uher, J.; Vykydal, Z. Pattern recognition of tracks induced by individual quanta of ionizing radiation in Medipix2 silicon detector. *Nucl. Instruments Methods Phys. Res. Sect. A Accel. Spectrometers Detect. Assoc. Equip.* **2008**, *591*, 287–290. [[CrossRef](#)]
39. Tensorflow. Available online: <https://www.tensorflow.org/> (accessed on 9 September 2023).
40. D’Agostini, G. Improved iterative Bayesian unfolding. *arXiv* **2010**, arXiv:1010.0632.
41. Brenner, L.; Verschuuren, P.; Balasubramanian, R.; Burgard, C.; Croft, V.; Cowan, G.; Verkerke, W. RooUnfold: ROOT Unfolding Framework. 2020. Available online: <https://gitlab.cern.ch/RooUnfold/RooUnfold> (accessed on 9 September 2023).
42. Kroupa, M.; Bahadori, A.A.; Campbell-Ricketts, T.; George, S.P.; Zeitlin, C. Kinetic energy reconstruction with a single layer particle telescope. *Appl. Phys. Lett.* **2018**, *112*, 134103. [[CrossRef](#)]
43. Kroupa, M.; Bahadori, A.A.; Campbell-Ricketts, T.; George, S.P.; Stoffle, N.; Zeitlin, C. Light ion isotope identification in space using a pixel detector based single layer telescope. *Appl. Phys. Lett.* **2018**, *113*, 174101. [[CrossRef](#)]
44. Agostinelli, S.; Allison, J.; Amako, K.; Apostolakis, J.; Araujo, H.; Arce, P.; Asai, M.; Axen, D.; Banerjee, S.; Barrand, G.; et al. Geant4—A simulation toolkit. *Nucl. Instruments Methods Phys. Res. Sect. A Accel. Spectrometers Detect. Assoc. Equip.* **2003**, *506*, 250–303. [[CrossRef](#)]
45. Garvey, D. Advanced Methodology for Radiation Field Decomposition with Hybrid Pixel Detectors. Master’s Thesis, Faculty of Nuclear Sciences and Physical Engineering, Czech Technical University in Prague, Prague, Czechia, 2023. Available online: <https://dspace.cvut.cz/handle/10467/108693> (accessed on 22 February 2024).
46. Michel, T.; Durst, J.; Jakubek, J. X-ray polarimetry by means of Compton scattering in the sensor of a hybrid photon counting pixel detector. *Nucl. Instruments Methods Phys. Res. Sect. A Accel. Spectrometers Detect. Assoc. Equip.* **2009**, *603*, 384–392. [[CrossRef](#)]
47. López Rosson, G.; Pierrard, V. Analysis of proton and electron spectra observed by EPT/PROBA-V in the South Atlantic Anomaly. *Adv. Space Res.* **2017**, *60*, 796–805. [[CrossRef](#)]
48. Farkas, M.; Bergmann, B.; Broulim, P.; Burian, P.; Ambrosi, G.; Azzarello, P.; Pušman, L.; Sitarz, M.; Smolyanskiy, P.; Sukhonos, D.; et al. Characterization of a Large Area Hybrid Pixel Detector of Timepix3 Technology for Space Applications. *Instruments* **2024**, *8*, 11. [[CrossRef](#)]
49. Jordan, C.E. RADEX INC BEDFORD MA, Contract No F19628-89-C-0068. Available online: <https://apps.dtic.mil/sti/citations/tr/ADA223660> (accessed on 26 October 2023).

50. Ginet, G.P.; O'Brien, T.P.; Huston, S.L.; Johnston, W.R.; Guild, T.B.; Friedel, R.; Lindstrom, C.D.; Roth, C.J.; Whelan, P.; Quinn, R.A.; et al. AE9, AP9 and SPM: New Models for Specifying the Trapped Energetic Particle and Space Plasma Environment. In *The Van Allen Probes Mission*; Fox, N., Burch, J.L., Eds.; Springer: Boston, MA, USA, 2014; pp. 579–615. [[CrossRef](#)]
51. Hulsmann, J.; Wu, X.; Azzarello, P.; Bergmann, B.; Campbell, M.; Clark, G.; Cadoux, F.; Ilzawa, T.; Kollmann, P.; Llopart, X. Relativistic Particle Measurements in Jupiter's Magnetosphere with Pix.PAN. *Exp. Astron.* **2023**, *56*, 371–402. [[CrossRef](#)]
52. Smolyanskiy, P.; Bergmann, B.; Burian, P.; Cherlin, A.; Jelínek, J.; Maneuski, D.; Pospíšil, S.; O'Shea, V. Characterization of a 5 mm thick CZT-Timepix3 pixel detector for energy-dispersive  $\gamma$ -ray and particle tracking. *Phys. Scr.* **2023**, *99*, 015301. [[CrossRef](#)]
53. Useche, S.J.; Roque, G.A.; Schütz, M.K.; Fiederle, M.; Procz, S. Characterization of a 5mm thick CdTe photon-counting detector: Advancing nuclear decommissioning with Compton camera technology. In Proceedings of the 2023 IEEE Nuclear Science Symposium, Medical Imaging Conference and International Symposium on Room-Temperature Semiconductor Detectors (NSS MIC RTSD), Vancouver, BC, Canada, 4–11 November 2023; p. 1. [[CrossRef](#)]

**Disclaimer/Publisher's Note:** The statements, opinions and data contained in all publications are solely those of the individual author(s) and contributor(s) and not of MDPI and/or the editor(s). MDPI and/or the editor(s) disclaim responsibility for any injury to people or property resulting from any ideas, methods, instructions or products referred to in the content.